In-Situ Liquefaction Testing of a Medium Dense Sand Deposit and Comparison to Case History- and Laboratory-based Cyclic Stress and Strain Evaluations

Armin W. Studlein[1[0000-0002-6265-9906]] and Amalesh Jana[2[0000-0003-1130-4037]]

[1] Oregon State University, Corvallis, OR 97331, USA
[2] Oregon State University, Corvallis, OR 97331, USA
armin.stuedlein@oregonstate.edu

Abstract. Observations of the dynamic loading and liquefaction response of a deep medium dense sand deposit to controlled blasting have allowed quantification of its large-volume dynamic behavior from the linear-elastic to nonlinear-inelastic regimes under *in-situ* conditions unaffected by the influence of sample disturbance or imposed laboratory boundary conditions. The dynamic response of the sand was shown to be governed by the *S-waves* resulting from blast-induced ground motions, the frequencies of which lie within the range of earthquake ground motions. The experimentally derived dataset allowed ready interpretation of the *in-situ* γ-u_e responses under the cyclic strain approach. However, practitioners have more commonly interpreted cyclic behavior using the cyclic stress-based approach; thus this paper also presents the methodology implemented to interpret the equivalent number of stress cycles, N_{eq}, and deduce the cyclic stress ratios, *CSRs*, generated during blast-induced shearing to provide a comprehensive comparison of the cyclic resistance of the *in-situ* and constant-volume, stress- and strain-controlled cyclic direct simple shear (DSS) behavior of reconstituted sand specimens consolidated to the *in-situ* vertical effective stress, relative density, and V_s. The multi-directional cyclic resistance of the *in-situ* deposit was observed to be larger than that derived from the results of the cyclic strain and stress interpretations of the uniaxial DSS test data, indicating the substantial contributions of natural soil fabric and partial drainage to liquefaction resistance during shaking. The cyclic resistance ratios, *CRRs*, computed using case history-based liquefaction triggering procedures based on the SPT, CPT, and V_s are compared to that determined from *in-situ* CRR-N_{eq} relationships considering justified, assumed slopes of the *CRR-N* curve, indicating variable degrees of accuracy relative to the *in-situ CRR*, all of which were smaller than that associated with the *in-situ* cyclic resistance.

Keywords: Liquefaction, in-situ testing, soil dynamics.

1 Introduction

Practitioners rely upon case history- and *in-situ* penetration resistance-based liquefaction triggering procedures owing to the availability of certain subsurface exploration techniques, the results of which can be obtained in the field where evidence of liquefaction has been observed. The basis for commonly used liquefaction triggering procedures rests with the observation that those factors affecting penetration resistance (e.g., relative density, overconsolidation, cementation) also and proportionally affect cyclic resistance (Boulanger and Idriss 2015). Such procedures provide an approximation of the cyclic resistance ratio, *CRR*, which in reality is complicated by transient, highly irregular multidirectional earthquake loading, inherent soil variability (Bong and Stuedlein 2018; Stuedlein et al. 2021), redistribution of excess pore pressure (Dobry and Abdoun 2015; Adamidis and Madabhushi 2018), and the system response of stratified deposits (Cubrinovski et al. 2019). Sampling soils in an undisturbed state and subsequent laboratory element tests have pointed to the role and importance of natural soil fabric on *CRR* (e.g., Yoshimi et al. 1984). However, sampling soils in an intact, relatively undisturbed state is difficult, particularly for clean and silty sands and gravels, and the true *in-situ* drainage boundary conditions may not be well-simulated in the laboratory (Dobry and Abdoun 2015). Numerous laboratory tests on reconstituted sand specimens have been conducted to understand how *CRR* varies with such factors as preparation technique, gradation, particle shape, among other variables; however, the major challenges associated with replicating the inherent or natural soil fabric and true stress and drainage boundary conditions in the field remains. Thus, the empirical correlations relating cyclic resistance to *in-situ* penetration resistance (e.g., Youd et al. 2001; Boulanger and Idriss 2014) and small-strain shear wave velocity, V_s, measurements (e.g., Andrus and Stokoe 2000; Kayen et al. 2013) continue to serve the profession with the most accessible means for the evaluation liquefaction triggering potential.

Advances in the characterization of the *in-situ* coupled, cyclic shear-induced excess pore pressure and nonlinearity of soil have been made using a mobile shaker truck (Rathje et al. 2001; Cox et al. 2009; Roberts et al. 2016). Mobile shaking of instrumented test panels allows for the direct observation of the soil response to known ground motions and represents an excellent technique for filling the gaps in the understanding of dynamic soil responses. However, the success of the surface loading technique is site-specific and necessarily restricted to shallow depths (typically 4 m or less; van Ballegooy et al. 2015). Another *in-situ* dynamic testing technique, controlled blasting, has been refined to obtain *in-situ* dynamic properties and successfully implemented in the deep medium dense sand deposit (25 m depth; Jana and Stuedlein 2021a) at the focus of this paper, and a medium-stiff silt deposit (Jana et al. 2021; Jana and Stuedlein 2021b) at a depth of 10 m. This paper describes the experimental, instrumented Sand Array, the blast liquefaction test programs conducted, the characterization of the observed ground motions, and the framework used to determine the blast-induced shear strains, shear stresses, and the corresponding equivalent number of stress cycles. Thereafter, this paper focuses on characterization of the *in-situ* relationships between shear strain, shear stress, and excess pore pressure generation interpreted within the cyclic stress and cyclic strain frameworks, and compares the *in-situ* responses to the results of cyclic direct simple shear tests conducted on representative reconstituted sand specimens retrieved from the Sand Array. The *in-situ* liquefaction resistance is shown to exceed that of the laboratory test specimens due to the natural soil fabric and field drainage, despite the application of multidirectional blast-induced ground motions. The paper concludes with a comparison of the *in-situ CRR* to that determined using SPT-, CPT-, and V_s-based liquefaction triggering procedures accompanied by a discussion of the influence of the assumed logarithmic slopes of the *CRR-N* curve implied by certain procedures and selected for the assessment of *in-situ* cyclic resistance. This paper demonstrates the utility of the controlled blasting technique to continue to advance our understanding of the dynamic, *in-situ*, deep liquefaction response of saturated sands.

2 Test Site and Geotechnical Conditions

The test site is situated just south of the Columbia River on the Port of Portland properties in Portland, Oregon (USA) and is underlain by soil deposits that pose potential seismic risk to the facilities owned and operated by the Port. Seismic hazards result in part from the proximity to the Portland Hills fault, located 10 km west, and the Cascadia Subduction Zone, located approximately 150 km west, of the site. Figure 1 presents the experimental layout and subsurface conditions, which consists of dredge sand and silty sand fill in the upper 5 to 6 m, underlain by a +/- 2 m thick layer of native, alluvial, loose, clean sand. The next layer consists of a 5 to 6 m thick alluvial, medium stiff, clayey silt (ML and MH) deposit characterized extensively in terms of its dynamic, *in-situ* and cyclic laboratory responses by Jana Stuedlein (2021a; 2021b). Extending below the silt layer and to the depth of the explorations lies a deep deposit of alluvial, medium dense sand forming the basis of the current study. The groundwater table varied approximately 3 to 7.3 m due to seasonal fluctuations of the adjacent river and nearby pumping throughout the course of the investigation.

Over the range in depths corresponding to the *in-situ* instrumentation, globally termed the Sand Array and ranging from 23.62 to 26.53 m, the sand layer is characterized as medium dense, poorly-graded fine sand (SP) and fine sand with silt (SP-SM), with fines content, *FC*, varying from 3.9% to 12.1% (average *FC* = 6%). The median grain size diameter, D_{50} of the sand ranges from 0.21 to 0.28 mm, with average coefficients of uniformity and curvature of 3.0 and 1.5, respectively. CPT test results indicate that I_c varies from 1.79 to 2.22, with an average I_c =1.9 within the Sand Array. The stress-normalized equivalent clean sand tip resistance, q_{c1Ncs} (Boulanger and Idriss 2014) of the sand layer varies from 83 to 108 with an average q_{c1Ncs} =98. SPT- and CPT-based estimates of relative density indicated a relative density, D_r, that generally ranges from 40 (derived via SPT; Cubrinovski and Ishihara 1999) to 47% (derived via CPT; Mayne 2007) over the instrumented depths.

3 Sand Array and Summary of the Dynamic *In-Situ* Test Program

The location of the Sand Array within the saturated, medium dense sand deposit is shown schematically in Figure 1, whereas the details regarding specific instruments and their geometry is presented in the Figure 2 inset. Two strings of three triaxial 28 Hz geophone packages (TGPs) accompanied with a six-axis accelerometer gyroscope to capture static tilt and extending from inclinometer casing, were each placed within 200 mm diameter mud-rotary boreholes (B-1 and B-3; Fig. 1) and grouted in place. One borehole was used to install a full-depth inclinometer casing fitted with sondex settlement rings to capture post-shearing volumetric strain (I-1, Fig. 1). Pore pressure transducers (PPTs; Fig. 2 inset) were installed in borehole B-2 (Fig. 1). The calibration of various instruments, installation procedure, borehole deviation survey, and identification of installed TGP locations and their orientations are described in Jana et al. (2021). The Sand Array was designed to form two rectangular elements which facilitated computation of the time-varying shear modulus, shear strain, and excess pore pressure developed within the instrumented soil mass using finite element methodology (Rathje et al. 2001; Cox et al. 2009). Each TGP functioned as a node of the rectangular finite element and allowed the computation of strain using integrated particle velocities, as described below.

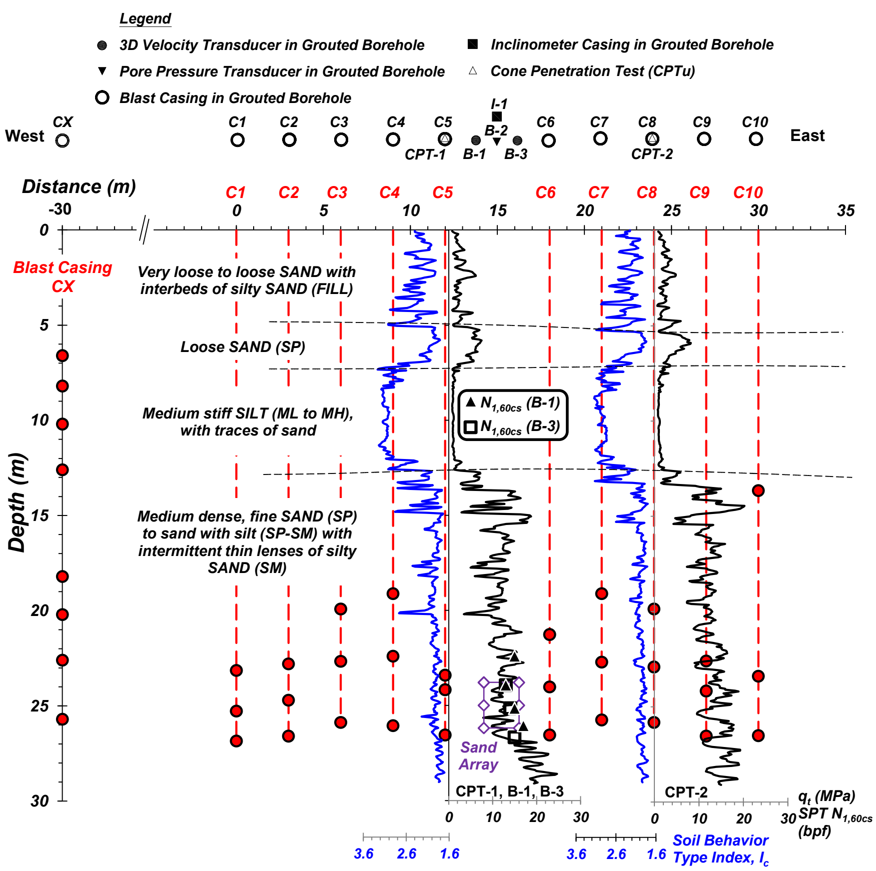

Fig. 1. Experimental layout for the Test (TBP) and Deep Blast Programs (DBP) and subsurface stratigraphy at the test site. Explosive charge locations are shown using red circular markers and the geophones comprising the Sand Array shown using purple diamond markers.

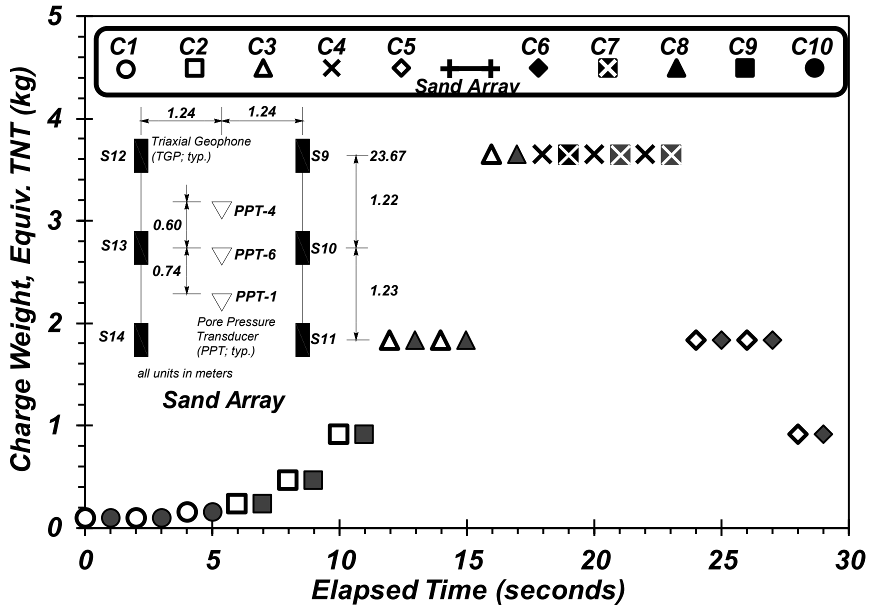

Fig. 2. Thirty-second detonation time history for the Deep Blast Program (DBP) and instruments comprising, and geometry of, the Sand Array centered at a depth of 24.9 m. Refer to Fig. 1 for location in plan and section.

Three *in-situ* dynamic tests using controlled blasting were performed in October 2018: the Test Blast (TBP), Deep Blast (DBP), and Shallow Blast Programs (SBP). The current study mainly focuses on the results from the DBP, the main goal of which was to load the Sand Array dynamically. The interested reader is referred to Jana and Stuedlein (2021a, 2021b) for additional and specific details of each of the blast events. Figure 1 presents a schematic illustrating the as-built position of each 30 charges detonated in the DBP and distributed using three charge decks within blast casings C1 through C10. Figure 2 indicates each detonation location and the sequence and charge weight (ranging from 90 grams to 3.65 kg) detonated, illustrating the sequential detonation program alternating from the east to the west of the Sand Array. This alternating pattern was selected to produce reverse dynamic loading of the Sand Array (i.e., alternating the polarity of maximum shear strains for each waveform). Figures 1 and 2 shows that the DBP initiated with small charges ~15 m from the center of the Sand Array, which increased in weight as the distance to the array reduced to the maximum charge weight, followed by a reduction in charge weight in proximity to the array at the end of the 30 s detonation program to prevent instrument damage.

4 Characterization and Interpretation of the Blast-Induced Ground Motions

4.1 Ground Motions

Blast-induced ground motions differ somewhat from earthquake-induced ground motions, and depend upon the source-to-site distance and charge weight. Beyond the zone of rapid gas expulsion in proximity to the charge, the ground motions consist of (Jana and Stuedlein 2021a): (1) a spherical- or cylindrical-shaped compressive shockwave (i.e., the *P*-wave) emanating from the charge location, depending on the length of the charge, (2) a longitudinally-propagating, shear or *S*-wave producing near-field shearing (longitudinal- or *x*-component dominant) that is generated from the unloading of the expanding shockwave within an anisotropic soil mass, and (3) and a vertically-polarized far-field *S*-wave (transverse- or *z*-component dominant) generated at the charge location. The near- and far-field *S*-wave may be superimposed depending on the ratio of the wavelength and source-to-site distance (Sanchez-Salinero et al. 1986).

Figure 3a presents an example of the vertical, *z*, and longitudinal, *x*, particle velocity time histories, V_z and V_x, measured in TGP S11 within the Sand Array (Fig. 2). Velocities increased from 0.033 to 1.002 m/s with reversal in the polarity of the maximum amplitude due to the alternating ray path from the charge locations. The V_z waveform for Blast #15 measured in TGP S11 is shown in Fig. 3b, illustrating the *P*-wave arrival followed by the near- and far-field *S*-waves. The near-field *S*-wave exhibits dominant particle motion in the *x*-direction, rather than the transverse (*z*) direction owing to its generation at the location of the unloading *P*-wave (Sanchez-Salinero et al. 1986). The displacements generated by the unloading of the *P*- and near-field *S*-waves, D_x and D_z, are significantly smaller than that of the far-field *S*-wave for this blast owing to their high frequencies (Jana and Stuedlein 2021a). The evolution of frequency, *f*, content of this blast-induced waveform may be visualized using the normalized Stockwell spectrum (Kramer et al. 2016) shown in Fig. 3c: the predominant frequency of the *P*-wave is f_P = 825 Hz, significantly higher than the near-field *S*-wave, $f_{S,nf}$ = 47 Hz, which is in turn three-fold larger than the far-field *S*-wave, with $f_{S,ff}$ = 15 Hz. Consequential displacements require low frequencies, regardless of the source of the ground motions; hence, the *P*-wave and its unloading is of little consequence when the charge is located sufficiently far from the point of observation. Furthermore, $f_{S,ff}$ lies within the range of typical earthquake-induced ground motions.

Figure 4a presents the Fourier spectra for the 30 blast-induced, full velocity waveforms of TGP S14z and the corresponding average normalized by their maximum Fourier amplitude. The predominant frequency of each record ranges from approximately 8 to 50 Hz, with higher frequencies occurring earlier in the blast program when the shear modulus of the sand, *G*, is relatively large (e.g., $G \approx G_{max}$). Note that the Fourier amplitudes for f_P are rather small in comparison to $f_{S,nf}$ and $f_{S,ff}$. The predominant *f* steadily reduces as the shear stiffness of the sand degrades and excess pore pressure, u_e, is triggered and accumulates (Jana and Stuedlein 2021c). Figure 4b compares the average normalized Fourier spectra for V_z observed in the TGPs comprising the Sand Array during DBP; the average predominant f is 13.4 Hz, indicative of the S-wave dominance of the blast-induced ground motions. In comparison, the average frequency of the P-waves is 1,185 Hz which travel at an average V_x of 1,559 m/s.

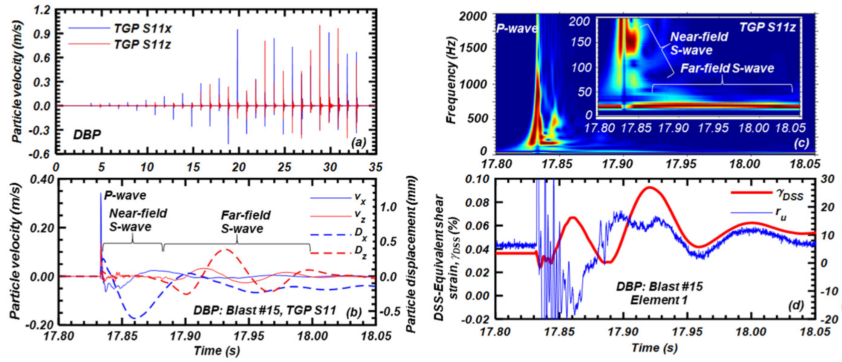

Fig. 3. Ground motions observed within the Sand Array: (a) example 30 s particle velocity time history of TGP S11, and characteristics of DBP Blast # 15 in terms of (b) particle velocity and corresponding displacement, (c) Stockwell spectrum of the of vertical component of motion (TGP S11z), and (d) variation of DSS-equivalent shear strain and excess pore pressure ratio.

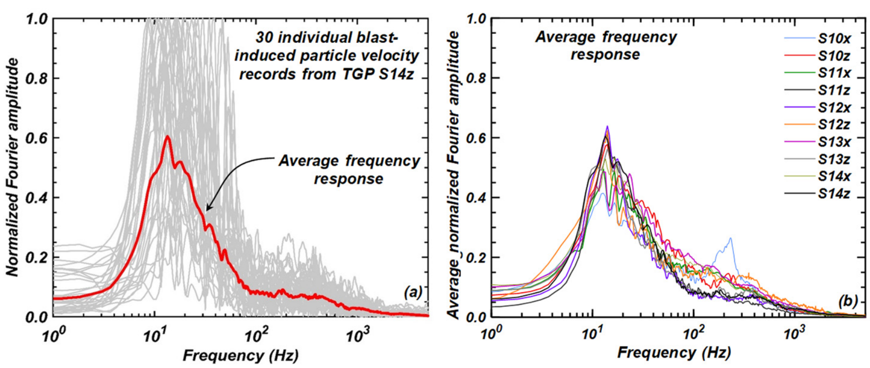

Fig. 4. Frequency content of the blast induced ground motions in the sand array during DBP: (a) normalized Fourier amplitude spectra for the 30 individual blast-induced particle velocity records for TGP S14z and the average response, and (b) average frequency response for the TGPs comprising the Sand Array.

4.2 Computation of Shear Strain

The geometry of the Sand Array allows formation of two isoparametric finite elements, termed Elements 1 and 2, which facilitate the calculation of shear strain, γ, from the integrated velocities. Element 1 is formed by TGPs S10, S11, S13, and S14, whereas Element 2 is formed by TGPs S9, S10, S12, and S13 (Fig. 2 inset). Shear strain is computed using the displacement-based finite element analyses proposed by Rathje et al. (2001) and successfully used in *in-situ* mobile shaking studies (Cox et al. 2009; Roberts et al. 2016). In this formulation, displacements D_x and D_z are used along with appropriate shape functions to deduce the 2D Cauchy strain tensor (i.e., normal strains ε_{xx}, ε_{zz}, and shear strain, γ_{xz}) corresponding to the mid-point of each element and the PPTs (Fig. 2). Although the strains computed using the selected method do not require plane waves, the majority of waveforms generated during the DBP may be assumed to pass as plane waves due to the geometry of the experiment and array (Jana and Stuedlein 2021a, 2021b). The Cauchy strain tensor is then used to compute the octahedral shear strain, γ_{oct}:

$$\gamma_{oct} = \left(\frac{2}{3}\right)\sqrt{(\varepsilon_{xx})^2 + (-\varepsilon_{zz})^2 + (\varepsilon_{zz} - \varepsilon_{xx})^2 + 6\left(\frac{\gamma_{xz}}{2}\right)^2} \tag{1}$$

which then allows comparison of the mobilized maximum *in-situ* strain with DSS test data by converting γ_{oct} to the DSS-equivalent, constant-volume shear strain, γ_{DSS}, through the imposition of plane strain boundary conditions on Eq. 1 (Cappa et al. 2017):

$$\gamma_{DSS} = \sqrt{\frac{3}{2}}\,\gamma_{oct} \tag{2}$$

which is strictly appropriate for 2D plane waves.

Figure 3d presents the computed γ_{DSS} and excess pore pressure ratio, r_u, time histories during Blast #15 in Element 1. The *P*-wave operates with a short wavelength of high frequency, and therefore does not provide an opportunity for movement of porewater during the period of loading and passes in a drained state (Ishihara 1967). For the experimental conditions in this experiment, the *P*-waves could not produce relative soil movement and corresponding residual excess pore pressure, u_{er} (Martin et al. 1975; Dobry et al. 1982; Jana and Stuedlein 2021a) within the Sand Array. Immediately following passage of the *P*-wave and coinciding with the unloading-induced near-field *S*-wave, u_e instantaneously returns to the pre-*P*-wave, ambient hydrostatic pressure (which varies over the course of a controlled blasting program as u_{er} accumulates). In contrast, the low frequency *S*-waves produced large displacements and corresponding γ_{DSS} and u_{er}; the excellent correspondence between γ_{DSS} and shear-induced u_{er} is evident in Fig. 3d. During Blast# 15, the maximum γ_{DSS}, $\gamma_{DSS,max}$, was 0.0926%, the maximum shear-induced r_u, $r_{u,max}$, was 17.6% and residual r_u, $r_{u,r}$ following the passage of the full waveform was 9.2%. The development of residual u_e, u_{er}, in the sand is associated with the gross sliding of the soil particles (Martin et al. 1975), which is associated with predominant *S*-wave during the passage of the blast pulse (Jana and Stuedlein 2021a). Equation (2) allows direct comparison to the strain-controlled cyclic DSS test data prepared from reconstituted specimens retrieved from the Sand Array, described below.

4.3 Computation of Shear Stress and Equivalent Number of Stress Cycles

Figure 5 presents an example waveform (Blast #30) measured at TGP S11z during the DBP. Since the *P*-wave passes in a drained state, and did not produce shear strain or u_{er} owing to its high frequency, the *P*-wave was removed from each particle velocity record using a low pass filter (Figs. 5a). The shear stress, τ, was then calculated from the filtered waveform using the methodology proposed by Joyner and Chen (1975) assuming that the propagating seismic wave can be represented as a plane wave, which was generally the case owing to the relative scales of the body wave front and the array (Jana and Stuedlein 2021a, 2021b), using:

$$\tau = \rho \cdot V \cdot V_s \tag{3}$$

where ρ = density. The strain dependent V_s was calculated from the crosshole response measured at each of the TGPs during the blast program for both longitudinal and transverse shear, justified by the negligible anisotropy in V_s as documented by Donaldson (2019). The corresponding cyclic (i.e, dynamic) shear stress ratio, *CSR*, is computed by normalizing the shear stress time history by σ'_{v0}, equal to 256 kPa and 231 kPa in Elements 1 and 2, respectively. Figure 5b presents the resulting *CSR* time history for Blast #30, indicating a maximum *CSR*, CSR_{max} = 0.13.

An algorithm to determine the equivalent number of stress cycles, N_{eq}, from the blast-induced particle velocities adapted from that developed for earthquake ground motions by Boulanger and Idriss (2004) was scripted within *matlab*. Each positive and negative half cycle, *i*, of the *CSR* time history is counted and the absolute maximum CSR_i of each half-cycle is stored. Then, the global maximum CSR_i is stored as CSR_{max}. If the ratio of CSR_i and CSR_{max} is less than 0.1 for any given half-cycle, the script removes the corresponding CSR_i and updates *i* for which the ratio of CSR_i and the CSR_{max} is more than 0.1 (Boulanger and Idriss 2004). The user can then input the reference cyclic stress ratio, CSR_{ref}, for which N_{eq} is to be calculated. In the next step, the script requires the exponent *b* of the power law describing the relationship between the cyclic resistance ratio, *CRR*, and the number of uniform cycles, *N*, $CRR = a{\cdot}N^{-b}$, assumed or derived from laboratory tests, as described below. Thereafter, the code computes the equivalent number of stress cycles for the blast pulse measured at a single TGP using (Boulanger and Idriss 2004):

$$N_{eq} = \frac{1}{2}\sum_{i=1}^{i}[(\frac{CSR_i}{CSR_{ref}})^{\frac{1}{b}}] \tag{4}$$

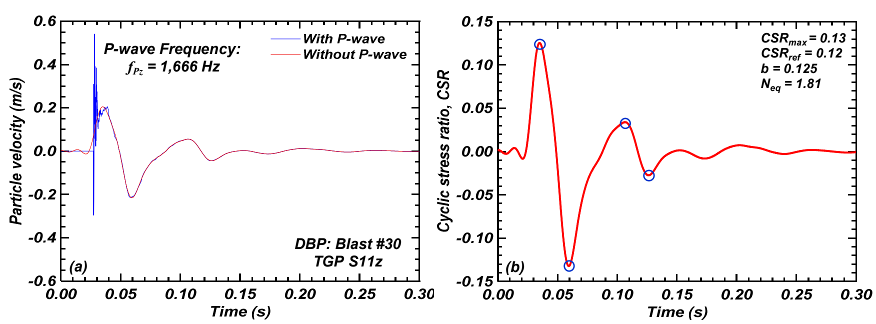

Fig. 5. Conversion of particle velocity to cyclic stress ratio for DBP Blast #30 registered in TGP S11z: (a) full waveform and filtered *z*-component particle velocity time histories, and (b) the corresponding *CSR* time history indicating CSR_{max} and the resulting N_{eq}.

Use of CSR_{ref} = 0.12 and b = 0.125, for example, results in N_{eq} = 1.81 for Blast #30 (Fig. 5b). The equivalent *CRR-N* curves for Elements 1 and 2 were developed by varying CSR_{ref} to obtain the corresponding average N_{eq} resulting from the average resultant *CSR* vector (i.e., from the longitudinal and transverse particle velocities) for each of the four TGPs comprising the element. This process was conducted for b = 0.125 and 0.28 to evaluate the role of the logarithmic slope of the assumed *CRR-N* power law for comparison to the DSS and case history-based cyclic resistances, as described in detail below.

5 *In-Situ* Cyclic Responses of the Medium Dense Sand Deposit and Comparison to Laboratory Behavior and Case History-based Liquefaction Procedures

5.1 Stress- and Strain-Controlled, Constant-Volume Laboratory Responses

The comparison of similarities and differences between certain dynamic *in-situ* and idealized laboratory element responses is facilitated herein through stress- and strain-controlled, constant-volume, cyclic direct simple shear (DSS) tests performed on reconstituted sand specimens collected from split-spoon samples. The typical height and diameter of sand specimens were 20 and 72 mm, respectively. Dry sand was air-pluviated in the membrane-lined DSS rings and consolidated to the *in-situ* vertical effective stress, $\sigma'_{v0} = \sigma'_{vc}$ = 240 kPa to achieve D_r = 51%, similar to that estimated from SPT- and CPT-based measurements, but necessary to obtain the same shear wave velocity, V_s = 218 m/s observed using bender elements within the DSS apparatus, as that measured using downhole tests in the Sand Array (Donaldson 2019; Jana and Stuedlein 2021a). Following consolidation, stress- and strain-controlled cyclic DSS tests were performed using uniform sinusoids of various constant stress and strain amplitudes at a frequency of 0.1 Hz.

Figures 6a – 6c present the results of stress-controlled cyclic DSS tests, indicating the shear stress-shear strain hysteresis in terms of the cyclic stress ratio, $CSR = \tau_{cyc}/\sigma'_{vc}$, development of shear strain, γ_{DSS}, and excess pore pressure ratio, r_u, with the number of loading cycles, N, and the cyclic resistance ratio, *CRR* with N. All of the specimens exhibited the cyclic failure, with greater *CSR*s resulting in greater γ_{DSS} and r_u for a given cycle of loading. For example, a specimen with CSR = 0.185 experienced a maximum γ_{DSS} = 1.54% to result in a residual excess pore pressure ratio, $r_{u,r}$, of 37.5%, compared to that with CSR = 0.146 with maximum γ_{DSS} = 1.01%, $r_{u,r}$ = 30% (Figure 6b). Herein, $r_{u,r}$ is defined as the ratio of u_e at the end of each loading cycle and σ'_{vc}. These two specimens reached γ_{DSS} = 3% in 2.7 and 11.6 cycles which corresponded to r_u = 70 and 90%, and r_u = 100% at N = 3.6 and 12.6, respectively. Figure 6c presents the *CRR-N* curve developed using all of the stress-controlled cyclic DSS test specimens, which may be represented using a power law of the form (Idriss and Boulanger 2008; Xiao et al. 2018:

$$CRR = aN^{-b} \tag{5}$$

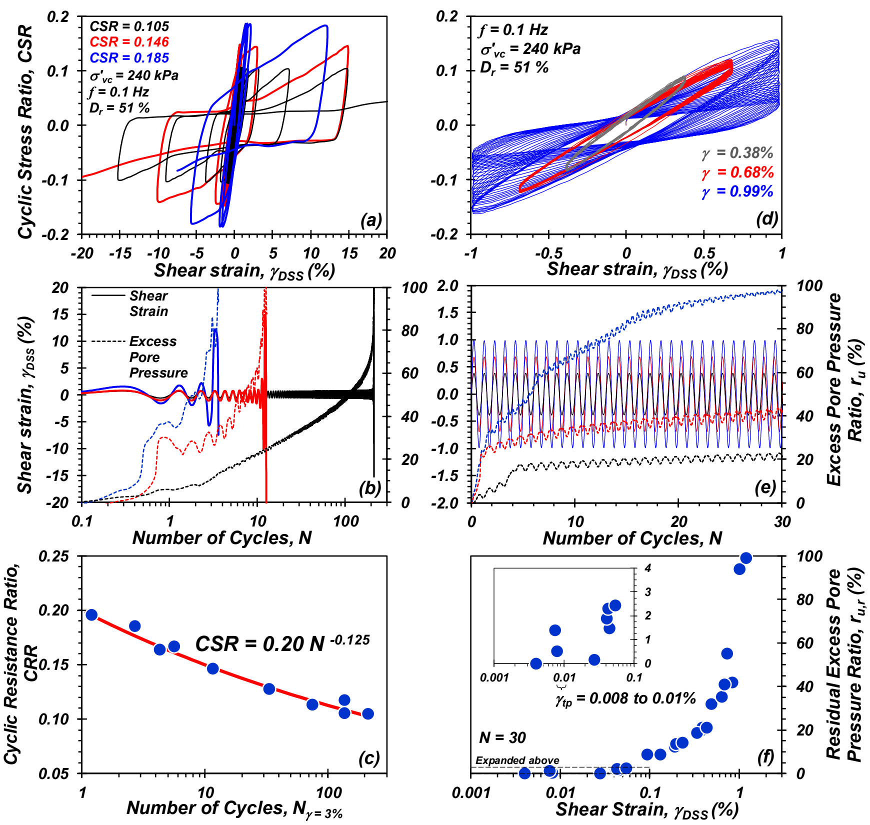

Fig. 6. Constant volume, cyclic direct simple shear test results on sand retrieved from the Sand Array: (a) sample stress-controlled hysteresis, (b) corresponding variation of shear, γ, strain and excess pore pressure ratio, r_u, with the number of cycles, N, (c) variation of cyclic stress ratio, CSR, with N for $\gamma = 3\%$, (d) sample strain-controlled hysteresis, (e) corresponding variation of γ and r_u with N, and (f) variation of γ with r_u.

where N = number of uniform loading cycles to reach 3% shear strain, and a and b are the fitted coefficient and exponent, respectively, with $a = 0.20$ and $b = 0.125$.

Figures 6d – 6f present the strain-controlled cyclic DSS test results conducted using $N = 30$. Larger imposed γ_{DSS} led to larger degradation in shear stiffness over the course of cyclic testing and corresponding greater r_u (Fig. 6e). The loops clearly exhibit the reduction of the secant shear modulus with N. The degradation is influenced by σ'_{vc} and f, where degradation is larger if σ'_{vc} is smaller and f, is higher (Mortezaie and Vucetic 2013). Figure 6f presents the variation of γ_{DSS} with $r_{u,r}$ for $N = 30$, indicating the threshold shear strain to trigger u_e, γ_{tp}, equal to about 0.008 to 0.01%, similar to that reported by Dobry and Abdoun (2015). This figure also indicates that $r_{u,r} \approx 100\%$ at $\gamma_{DSS} \approx 1\%$ ($N = 30$).

5.2 *In-Situ* Seismic Response Observed within the Sand Array

The dataset developed from the Deep Blast Program provides an unprecedented view of the dynamic response of saturated, medium dense sands to blast-induced ground motions. Figure 7 presents examples of the full *CSR* (Figs. 7a and 7b), DSS-equivalent shear strain (Fig. 7c), and corresponding excess pore pressure (Fig. 7d) time histories observed during the DBP, indicating correspondence between the gradually increasing *CSR*s and the development of γ_{DSS} and r_u. The excess pore pressure time history displays the high frequency *P*- and *S*-wave-induced u_e (termed "dynamic," Fig. 7d) as well as a representation of the accumulated u_e, for ease of interpretation. The first several charges produced *CSR*s of approximately 0.02 or less, resulting in very little accumulated γ_{DSS} and no $u_{e,r}$ in the case of the first two and three charges for Elements 1 and Element 2. As the charge weights and corresponding *CSR*s increased, γ_{tp} was exceeded to produce non-zero $r_{u,r}$ which accumulated steadily with each additional charge. The maximum *CSR* during the DBP was approximately 0.36 measured using TGP S14 (not shown), associated with a small charge located approximately 3 m from the center of the Sand Array, compared to 0.313 and 0.223 in TGPs S10 and S11 (Figs. 7a and 7b).

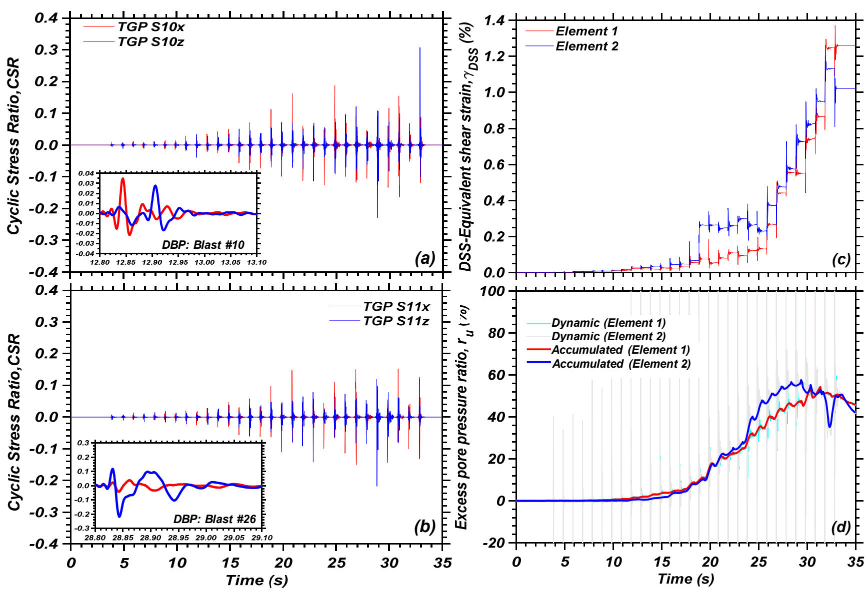

Fig. 7. Time histories of the seismic response observed within the Sand Array, including cyclic stress ratios for: (a) TGP S10, with inset showing Blast #10, (b) TGP S11, with inset showing Blast #26, (c) DSS-equivalent shear strain, and (d) excess pore pressure.

Figure 7 shows that the relationship between the non-uniform blast-induced *CSR*s and r_u is somewhat difficult to discern. In comparison, there appears to be a direct relationship between γ_{DSS} and r_u, with increasing strains leading directly to increased accumulation of excess pore pressures. The maximum γ_{DSS}, $\gamma_{DSS,max}$, observed during the

DBP was 1.371 and 1.200% for Elements 1 and 2, respectively, associated with $r_{u,max}$ and $r_{u,r}$ of 64 and 53%, and 72 and 57%, respectively. Apparent in Fig. 7d, drainage within the Sand Array initiated during Blast #26 in Element 2 and Blast #28 in Element 1. The 3D excess pore pressure field generated by the blast program initiated hydraulic gradients that were sufficiently large to lower the u_e within the Sand Array. The partial drainage led to the development of smaller γ_{DSS} than would have been expected for a fully-undrained response, and was accompanied by a smaller reduction in the large-strain shear modulus as described in Jana and Stuedlein (2021a). Although this observation provides additional evidence for the effect of partial drainage during shaking to provide greater shearing resistance and stiffness (e.g., Adamidis et al. 2019; Ni et al. 2021), the 3D u_e field generated during the DBP differs from that anticipated under earthquake ground motions.

5.3 Comparison of *In-Situ* and Strain- and Stress-controlled Laboratory Responses

One of the main goals of the controlled blasting test program at the Port of Portland site was to establish the *in-situ* dynamic response of natural, medium dense sands towards improving the assessment of the liquefaction hazard at the site. The main benefits of direct *in-situ* testing is that the soil response can be observed under its existing stress state within a large volume, without the detrimental effects of sample disturbance on the natural soil fabric, developed over thousands of years at this site, and without artificially-imposed boundary conditions. Side-by-side comparison of the *in-situ* and laboratory element test results serve identify similarities and differences and the role of natural soil fabric on the seismic response of liquefiable sands.

Comparison of the *in-situ* and laboratory element test results within the framework of the cyclic strain method (Dobry et al. 1982; Dobry and Abdoun 2015) first requires pairing the $r_{u,r}$ associated with each blast pulse to the corresponding $\gamma_{DSS,max}$. The use of 1 s delays between detonations allowed for the ready identification of $r_{u,r}$, which is defined as the excess pore pressure ratio in the quiescent period following passage of any given *S-wave* and immediately prior to the arrival of the following blast pulse. Figure 8a presents the variation of $\gamma_{DSS,max}$ with $r_{u,r}$ observed during the TBP (provided here to indicate the linear- and nonlinear-elastic responses) and the DBP. The TBP and DBP indicate $r_{u,r}$ of approximately 0.1 to 0.3% for $\gamma_{DSS,max} = \gamma_{tp}$ ranging 0.008% and 0.010% during the Test and Deep Blast Programs (Fig. 8a inset), consistent with the strain-controlled DSS tests on the reconstituted specimens with N = 30 and the previously reported γ_{tp} summarized by Dobry and Abdoun (2015) for laboratory element, centrifuge, large-scale laboratory, and field tests with $50 \leq \sigma'_{v0} \leq 200$ kPa. *In-situ* shear strains exceeding γ_{tp} resulted in a rapid rise in the $r_{u,r}$ observed in Element 1, with a somewhat more gradual rise in Element 2 over the range of $\gamma_{tp} \leq \gamma_{DSS,max} \leq 0.3\%$. Thereafter, excess pore pressure within Element 1 may have migrated upwards into Element 2 during the remainder of the DBP and $r_{u,r}$ in Element 2 increased more rapidly with $\gamma_{DSS,max} \leq 0.7\%$. Further increases in shear strain appear to have been arrested due to the drainage established under the 3D u_e field. In contrast, the laboratory element test results indicate a similar, though more gradual, rise in $r_{u,r}$ for $\gamma_{DSS} \leq 0.8\%$; larger shear strains resulted in continued increases in $r_{u,r}$ to ~100% corresponding to $\gamma_{DSS} \approx 1\%$ due to the imposed constant-volume conditions. Whereas the *in-situ* and strain-controlled cyclic DSS tests on the reconstituted sand specimens consolidated to the *in-situ* σ'_{v0}, D_r, and V_s agreed well, the differences observed for larger strains could result from the effect of multi-directional loading, differences in the soil fabric, and the redistribution and upward migration of u_e, or a combination of these effects.

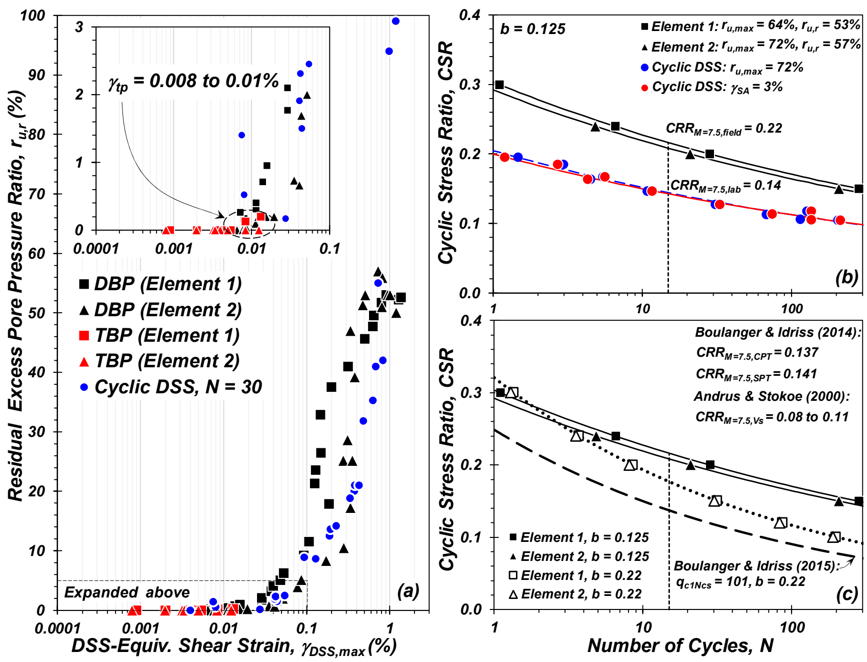

Fig. 8. Comparison of laboratory and *in-situ* test-based cyclic and dynamic responses: (a) variation of residual excess pore pressure with strain-controlled, constant-volume cyclic DSS and blast-induced DSS-equivalent maximum shear strain, (b) variation of stress-controlled, cyclic DSS and blast-induced cyclic stress ratios with the number of cycles for various cyclic performance criteria, and (c) comparison of CPT-based cyclic resistance ratios with the *in-situ,* controlled blasting-based *CRR*s for laboratory and assumed *b* exponents.

Figure 8b presents the comparison of the variation of *CSR* with *N* and N_{eq} for two liquefaction failure criteria and for the *in-situ* or field conditions and constant-volume, stress-controlled DSS tests at the same σ'_{v0}, D_r, and V_s. The field *CRR*-*N* curve shown in Fig. 8b corresponds to $b = 0.125$, equal to that determined from the stress-controlled cyclic DSS tests (Fig. 6b), for the purposes of comparison. Owing to the observed $r_{u,max}$ < 95 to 100%, the laboratory test data was reinterpreted to compare differences in the cyclic resistance ratio, *CRR*, at $\gamma_{DSS} = 3\%$ and $r_{u,max} = 72\%$, the maximum observed in the Sand Array. Figure 8b shows that the differences between these two cyclic failure criteria are negligible, with nearly identical *CRR-N* curves over the available range in

N. Comparison to the field-measured *in-situ CRR* with the laboratory-based cyclic resistance at $r_{u,max}$ = 72% is therefore reasonable. Figure 8b shows that (1) the field *CRR*-*N* curve for Element 1 is higher than that of Element 2, owing to the lower excess pore pressures developed, and (2) the *in-situ* sand exhibits significantly larger liquefaction resistance than that of the reconstituted sand specimens at a given *N*. For example, for *N* = 15 and corresponding to M_w = 7.5, the *in-situ CRR* = 0.22 is ~50% larger than that of the laboratory specimens (*CRR* = 0.22), which has not been reduced to account for the effects of multi-directional shaking. This result agrees well with the laboratory cyclic resistances determined on frozen and cored, and unfrozen sampled sands with $D_r \approx$ 50% reported by Yoshimi et al. (1984). Given that partial drainage occurred during the last stages of the DBP, it is likely that the *in-situ* cyclic resistance benefitted from both the effects of drainage and its natural soil fabric.

Table 1. Threshold shear strain to trigger liquefaction for M_w = 7.5 computed for the Sand Array within the cyclic strain framework.

Element	Blast Program	Vertical effective stress σ'_{v0} (kPa)	*In-situ* downhole V_s / V_{s1} (m/s)	Reference shear strain, γ_r (%)	Threshold shear strain to trigger liquefaction, γ_{cl} (%)
1	Prior to TBP	256	225 / 178	0.042[1] / 0.066[2]	0.139[3] / 0.071[4]
	Prior to DBP	256	192 / 151		0.087 / 0.054
2	Prior to TBP	231	218 / 177	0.040 / 0.089	0.123 / 0.053
	Prior to DBP	231	210 / 170		0.104 / 0.049

[1, 3] γ_r derived using Darendeli (2001)
[2, 4] γ_r derived using Menq (2003)

5.4 Comparison of the *In-Situ* Response to the Case History-based Cyclic Strain and Stress Liquefaction Triggering Procedures

The suite of in-situ tests (SPT, CPT, V_s) and constant-volume, cyclic DSS element tests conducted on specimens prepared from split-spoon samples retrieved within the Sand Array provide the basis for comparison to the liquefaction resistance estimated using the case history-based cyclic strain and stress liquefaction procedures. The threshold shear strain to trigger liquefaction, γ_{cl}, was computed using the V_s-based cyclic strain framework updated by Dobry and Abdoun (2015) for a M_w = 7.5 earthquake scenario using the downhole V_s measured within the Sand Array, as summarized in Table 1. Dobry and Abdoun (2015) use the Andrus and Stokoe (2000) case history-based *CRR*-V_{s1} curve to link γ_{cl} to *CRR*. Estimation of γ_{cl} requires the use of shear modulus reduction curves, such as those proposed by Darendeli (2001) and Menq (2003), and the corresponding reference shear strain, γ_r, defined as the shear strain associated with one-half G_{max} (Table 1). Note that V_s reduced by approximately 3.5 and 10% in Elements 1 and 2, respectively, following the TBP, which was attributed to the largest magnitude of $\gamma_{DSS,max}$ imposed on Elements 1 and 2 during the TBP (Fig 8a) and which just exceeded γ_{tp} in Element 1 (Jana and Stuedlein 2021a). The γ_{cl} for the conditions just prior to the

DBP ranges from 0.049 to 0.104% for the two elements, approximately 10 times smaller than the strains giving rise to $r_{u,max}$ (64 and 72% for Elements 1 and 2, respectively). This may be attributed to the effect of partial drainage and/or lack of correspondence of the DBP to the loading associated with a M_w = 7.5 earthquake.

The cyclic resistance of the medium dense sand within the Sand Array was computed using case history- and *in-situ* test-based liquefaction triggering procedures set within the cyclic stress method, including those based on the SPT and CPT (Boulanger and Idriss 2014) and V_s (Andrus and Stokoe 2000) for comparison to resistance determined from the DBP. The previous comparison to laboratory test results on reconstituted DSS test specimens produced the *CRR-N* exponent b = 0.125; however, the laboratory test results were shown to under-predict the field *CRR-N* curve as described above. Boulanger and Idriss (2004) selected b = 0.34 for clean sand based on the results of cyclic tests on frozen samples reported by Yoshimi et al. (1984). In reality, b can vary significantly for sands depending on the relative density, soil fabric, cementation, and other factors (Boulanger and Idriss 2015; Verma et al. 2019; Zamani and Montoya 2019). This prompted revision to the CPT- and SPT-based liquefaction triggering procedures (Boulanger and Idriss 2014, 2015) based on experimental data from the literature showing that the negative logarithmic slope of the *CRR-N* curve, b, tended to increase with relative density as expressed through q_{c1Ncs}. Based on the updated relationship, the exponent b corresponding the material comprising the Sand Array (with average q_{c1Ncs} = 98) is approximately 0.22. Figure 8c clearly shows that the implied field *CRR* depends on the assumed magnitude of b, with notable disagreement in the CRR-N curves for large N (e.g., 24% at N = 30). Future blast-liquefaction tests may help to provide further guidance on relationships between penetration resistance, b, and the *in-situ CRR*.

Table 2 presents *CRR*s corresponding to b = 0.125 (laboratory) and 0.22 (CPT) for comparison to the case history- and *in-situ* test-based *CRR*s. The case history- and *in-situ* test-based *CRR*s were computed using average penetration resistances (see Section 2) and method-specific overburden stress correction factors, K_σ, where applicable and for M_w = 7.5 (i.e., N = 15). Table 2 summarizes the range in *CRR*s, which indicates that the V_s-based cyclic resistances, ranging from 0.08 to 0.11, fall well below that estimated from the controlled blasting program when considering either b exponent. This is significant, as the measured $r_{u,max}$ (i.e., 72%) and $\gamma_{DSS,max}$ (1.37%) within the Sand Array was smaller than that typically attributed to liquefaction triggering within the simplified procedure (i.e., $r_{u,max}$ = 95 to 100%, γ_{DSS} = 3%). The SPT-based triggering procedure returned $CRR_{M=7.5}$ = 0.141, approximately 20 and 34% smaller than the field $CRR_{M=7.5}$ for b = 0.22 and 0.125, respectively. Similarly, the $CRR_{M=7.5}$ computed using the CPT-based procedure returns *CRR*s that are 22 and 36% of that determined from the DBP and corresponding estimates of b. Differences in the available case histories used for the Andrus and Stokoe (2000) procedure and specific calibration decisions appear responsible for the differences between the V_s and penetration resistance-based *CRR*s summarized in Table 2. Note that the *CRR* calculated for the Sand Array using the CPT-based procedure implemented the mean q_{c1Ncs} corrected using the global I_c-FC correlation accompanying the Boulanger and Idriss (2014) model (*n.b.*, SPT-based *CRR* used actual *FC*). Use of the mean *FC* from the split-spoon samples (~6%) with the CPT-based procedure returned CPT-based *CRR* of 0.106, closer to the V_s-based *CRR* and

25% lower than the comparable SPT-based procedure. Thus, consideration should be given to how *FC* corrections to *CRR* are made within the framework of the procedure-specific calibrations and what the impact could be to estimated cyclic resistance.

The comparison summarized in Table 2 underlines the observation that the *in-situ* cyclic resistance, regardless of the reasonably assumed power law parameter *b*, is 20% greater or more than that determined using the case history-based liquefaction triggering procedures and that *in-situ* testing can provide distinct advantages for those considering risk and mitigation of liquefaction hazards.

Table 2. Comparison of the case history-based cyclic resistance for M_w = 7.5 (N = 15) to the *in-situ* cyclic resistance for the Sand Array for the DBP.

In-Situ Test Method	Reference	Resistance Term	Overburden Stress Correction, K_σ	$CRR_{M=7.5}$
SPT	Boulanger and Idriss (2014)	$N_{1,60cs}$ = 15 bpf	0.90	0.141
CPT	Boulanger and Idriss (2015)	q_{c1Ncs} = 98[1]	0.88	0.137
V_s	Andrus and Stokoe (2000)	V_{s1} = 151 to 170 m/s	N/A	0.08 to 0.11
Controlled Blasting	This study	b = 0.125 b = 0.22	N/A	0.215 0.177

[1] using method-specific global CPT-based I_c-*FC* correlation; q_{c1Ncs} = 68 and *CRR* = 0.106 when using mean *FC* from split-spoon samples

6 Concluding Remarks

The results of a blast-liquefaction test program conducted within a natural deposit of saturated, medium dense sand at a depth of 25 m are presented to demonstrate its dynamic response *in-situ* free of the effects of sample disturbance and imposed stress and drainage boundary conditions. Comparison to the response of laboratory test specimens reconstituted from samples retrieved from the same depths allow the identification of similarities and differences between the cyclic responses. The *in-situ* cyclic resistance determined through the assessment of the equivalent number of stress cycles associated with the blast-induced ground motions is compared to that computed using case history- and *in-situ* test-based liquefaction triggering procedures, allowing for direct assessment of their accuracy. The following conclusions may be drawn from this study:

1. Under the experimental conditions (e.g., charge weights, source-to-site distances) described herein, the dynamic response of the sand was controlled by *S-waves* with predominant frequencies falling within the range of earthquake ground motions. The frequency content of the *P-waves* is too large to produce appreciable displacements and strains, and therefore residual excess pore pressures, $u_{e,r}$, are controlled by low-frequency *S-waves*.

2. Dynamic shear stresses were computed for the blast-induced motions considering their largely two-dimensional nature at the experimental scale implemented, enabling quantification of the corresponding shear stress time histories. Application of the widely-used procedures to determine the equivalent number of shear stress cycles, N_{eq}, for transient earthquake ground motions were adapted to compute the corresponding N_{eq} for the blast motions.
3. Whereas the relationship between the *CSR*s and u_e was difficult to discern within the cyclic stress framework, a direct link between γ_{DSS} and $r_{u,r}$ was observed and supported previous conclusions regarding the advantages of the cyclic strain framework.
4. The multi-directional *in-situ* cyclic resistance interpreted within the cyclic stress and strain frameworks was observed to be greater than that quantified with uniaxial cyclic loading of reconstituted sand specimens consolidated to the *in-situ* σ'_{v0}, D_r, and V_s, serving to demonstrate the role of natural soil fabric and field drainage on liquefaction resistance.
5. The *in-situ* or field *CRR* depends on the assumed magnitude of the logarithmic slope of the *CRR-N* curve, *b*, suggesting that further refinement of the relationships between dynamic *in-situ* and cyclic laboratory test results are warranted.
6. Comparison of the field *CRR*s computed using reasonable *CRR-N* power law exponents *b* to those computed using case history- and *in-situ* test-based liquefaction triggering procedures indicated significant variability in their accuracy. The selected V_s-based *CRR* was up to 50% lower than that computed for the field, whereas the CPT- and SPT-based *CRR*s were 20 to 36% lower. Differences in the procedure-specific calibrations and/or available case histories appear responsible for these differences.

When coupled with the selected instrumentation scheme, controlled blasting offers an alternative method for the assessment of *in-situ* cyclic resistance unaffected by soil disturbance or imposed drainage boundary conditions, and may be readily interpreted within the cyclic stress and strain frameworks. The technique described herein can serve to further deepen the understanding of the seismic response of a wide range in geotechnical materials.

7 Acknowledgements

The authors gratefully acknowledge the sponsorship of this work by the Cascadia Lifelines Program (CLiP) and its members, with special thanks to sponsoring member agency Port of Portland and Tom Wharton, P.E. The authors were supported by the National Science Foundation (Grant CMMI 1663654) on this and similar work during the course of these experiments. The authors gratefully acknowledge the numerous individuals aiding in discussions and collaborative parallel work over the course of this study. The views presented herein represent solely those of the authors.

References

1. Adamidis, O., Madabhushi, S.P.G.: Experimental investigation of drainage during earthquake-induced liquefaction. Geotechnique 68(8), 655–665 (2018).

2. Adamidis, O., Sinan, U., Anastasopoulos, I.: Effects of partial drainage on the response of Hostun sand: an experimental investigation at element level. Earthquake Geotechnical Engineering for Protection and Development of Environment and Constructions, 4, 993-1000 (2019).
3. Andrus, R.D., Stokoe, K.H. II.: Liquefaction resistance of soils from shear-wave velocity. J. Geotech. Geoenv. Eng. 126 (11) 1015–1025 (2000).
4. Bong, T., Stuedlein, A.W.: Effect of Cone Penetration Conditioning on Random Field Model Parameters and Impact of Spatial Variability on Liquefaction-induced Differential Settlements. J. Geot. Geoenv. Eng. 144, (5), 04018018 (2018).
5. Boulanger, R.W., Idriss, I.M.: CPT and SPT Based Liquefaction Triggering Procedures. In: Report No. UCD/CGM-14/01, pp. 138, UC Davis, California (2014).
6. Boulanger, R.W., Idriss, I.M.: Evaluating the potential for liquefaction or cyclic failure of silts and clays. In: Report No. UCD/CGM-04/01, pp. 131, UC Davis, California (2004).
7. Boulanger, R.W., Idriss, I.M.: Magnitude scaling factors in liquefaction triggering procedures. Soil Dyn. Earthq. Eng. 79, 296-303 (2015).
8. Cappa, R., Brandenberg, S.J., Lemnitzer, A.: Strains and pore pressures generated during cyclic loading of embankments on organic soil. J. Geot. Geoenv. Eng. 143(9), 04017069 (2017).
9. Cox, B.R., Stokoe, K.H. II, Rathje, E.M.: An in -situ test method for evaluating the coupled pore pressure generation and nonlinear shear modulus behavior of liquefiable soils. Geotechnical Testing Journal 32(1), 11-21 (2009).
10. Cubrinovski, M., Ishihara, K.: Empirical correlation between SPT N-value and relative density for sandy soils. Soils and Foundations 39(5), 61-71 (1999).
11. Cubrinovski, M., Rhodes, A., Ntritsos, N., Van Ballegooy, S., System response of liquefiable deposits. Soil Dynamics and Earthquake Engineering 124, 212-229 (2019).
12. Darendeli, M.B.: Development of a new family of normalized modulus reduction and material damping curves. PhD Thesis, Univ. of Texas at Austin, Austin, Texas (2001).
13. Dobry, R., Abdoun, T.: Cyclic shear strain needed for liquefaction triggering and assessment of overburden pressure factor K_σ. J. Geot. Geoenv. Eng. 141(11), 04015047 (2015).
14. Dobry, R., Ladd, R.S., Yokel, F.Y., Chung, R.M., Powell, D.: Prediction of pore water pressure buildup and liquefaction of sands during earthquakes by the cyclic strain method. National Bureau of Standards Report 138. Gaithersburg, MD (1982).
15. Donaldson, A.M.: Characterization of the Small-Strain Stiffness of Soils at an In-situ Liquefaction Test Site. MS Thesis, pp. 287, Oregon State University (2019).
16. Idriss, I.M., Boulanger, R.W. Soil Liquefaction during Earthquakes. In: EERI Monograph No. 12, Earthquake Engineering Research Institute, pp. 237 (2008).
17. Ishihara, K.: Propagation of compressional waves in a saturated soil. In: Proc. Int. Symp. Wave Prop. Dyn. Prop. Earth Mat., Univ. of New Mexico Press, Albuquerque, NM, 195-206 (1967).
18. Jana, A. Stuedlein, A.W.: Dynamic, In-situ, Nonlinear-Inelastic Response of a Deep, Medium Dense Sand Deposit. J. Geot. Geoenv. Eng. 147(6), 04021039 (2021).
19. Jana, A. Stuedlein, A.W.: Dynamic, In-situ, Nonlinear-Inelastic Response and Post-Cyclic Strength of a Plastic Silt Deposit. Can. Geot. J. In Press (2021).
20. Jana, A., Donaldson, A. M., Stuedlein, A. W., Evans, T. M.: Deep, In Situ Nonlinear Dynamic Testing of Soil with Controlled Blasting: Instrumentation, Calibration, and Application to a Plastic Silt Deposit. Geotechnical Testing Journal 44(5) (2021).
21. Joyner, W.B., Chen, A.T.: Calculation of nonlinear ground response in earthquakes. Bull. Seis. Soc. Am., 65(5), 1315-1336 (1975).

22. Kayen, R., Moss, R. E. S., Thompson, E. M., Seed, R. B., Cetin, K. O., Kiureghian, A. D., Tokimatsu, K.: Shear-wave velocity–based probabilistic and deterministic assessment of seismic soil liquefaction potential. J. Geot. Geoenv. Eng. 139(3), 407-419 (2013).
23. Kramer, S.L., Sideras, S.S., Greenfield, M.W.: The timing of liquefaction and its utility in liquefaction hazard evaluation. Soil Dyn. Earthq. Eng. 91, 133-146 (2016).
24. Martin, G.R., Finn, W.D.L., Seed, H.B.: Fundamentals of liquefaction under cyclic loading. J. Geot. Eng. Div. 101(5), 423-438 (1975).
25. Mayne, P.W.: Cone penetration testing: A synthesis of highway practice. NCHRP Report, No. 368. Transportation Research Board, Washington, D.C. (2007).
26. Menq, F.Y.: Dynamic properties of sandy and gravelly soils. PhD Thesis, University of Texas, Austin (2003).
27. Mortezaie, A. R., & Vucetic, M.: Effect of frequency and vertical stress on cyclic degradation and pore water pressure in clay in the NGI simple shear device. J. Geotech. Geoenv. Eng., 139(10), 1727-1737 (2013).
28. Ni, M., Abdoun, T., Dobry, R., El-Sekelly, W.: Effect of Field Drainage on Seismic Pore Pressure Buildup and Kσ under High Overburden Pressure. J. Geot. Geoenv. Eng. 147(9), 04021088 (2021).
29. Rathje, E.M., Phillips, R., Chang, W.J., Stokoe, K.H. II: Evaluating Nonlinear Response In Situ, In: Proceedings of 4th Int. Conf. on Recent Adv. Geot. Earthq. Eng. Soil Dyn., San Diego, CA (2001).
30. Roberts, J.N., Stokoe, K.H II, Hwang, S., Cox, B.R., Wang, Y., Menq, F.M., van Ballegooy, S.: Field measurements of the variability in shear strain and pore pressure generation in Christchurch soils. In: Proc., 5th Int. Conf. on Geot. Geophys. Site Char. (2016).
31. Sanchez-Salinero, I., Roesset, J.M., Stokoe, K.H. II: Analytical Studies of Wave Propagation and Attenuation. In: Report, Air Force Office of Scientific Research, Bolling AFB, Washington, D.C., pp. 296 (1986).
32. Stuedlein, A.W., Bong, T., Montgomery, J., Ching, J., Phoon, K.K.: Effect of Densification on the Random Field Model Parameters of Liquefiable Soil and their Use in Estimating Spatially-distributed Liquefaction-induced Settlement. International Journal of Geoengineering Case Histories, (2021). *In Press.*
33. Van Ballegooy, S., Roberts, J. N., Stokoe, K. H., Cox, B. R., Wentz, F. J., Hwang, S.: Large-scale testing of shallow ground improvements using controlled staged-loading with T-Rex. In Proceedings of the 6th International Conference on Earthquake Geotechnical Engineering, pp. 1-4, Christchurch, New Zealand (2015).
34. Verma, P., Seidalinova, A., Wijewickreme, D.: Equivalent number of uniform cycles versus earthquake magnitude relationships for fine-grained soils. Can. Geot. J., 56(11), 1596-1608 (2019).
35. Xiao, P., Liu, H., Xiao, Y., Stuedlein, A.W., Evans, T.M., Jiang, X.: Liquefaction Resistance of Bio-cemented Calcareous Sand. Soil Dyn. Earthq. Eng., 107, 9-19 (2018).
36. Yoshimi Y., Tokimatsu, K., Kaneko, O., Makihara, Y.: Undrained cyclic shear strength of a dense Niigata sand. *Soils Found.*, 24(4), 131-145 (1984).
37. Youd, T. L., Idriss, I. M.: Liquefaction resistance of soils: summary report from the 1996 NCEER and 1998 NCEER/NSF workshops on evaluation of liquefaction resistance of soils. J. Geot. Geoenv. Eng., 127(4), 297-313(2001).
38. Zamani, A., Montoya, B.M.: Undrained cyclic response of silty sands improved by microbial induced calcium carbonate precipitation. Soil Dyn. Earthq. Eng., 120, 436-448 (2019).